

DISCOVERY OF KILOHERTZ FLUCTUATIONS IN CENTAURUS X-3: EVIDENCE FOR PHOTON BUBBLE OSCILLATIONS (PBO) AND TURBULENCE IN A HIGH-MASS X-RAY BINARY PULSAR

J. GARRETT JERNIGAN,¹ RICHARD I. KLEIN,^{2,3,5} AND JONATHAN ARONS^{2,4,5}

Received 1999 April 5; accepted 1999 October 10

ABSTRACT

We report the discovery of kilohertz fluctuations, including quasiperiodic oscillations (QPO) at ~ 330 Hz (260–407 Hz) and ~ 760 Hz (671–849 Hz) and a broadband kilohertz continuum in the power-density spectrum of the high-mass X-ray binary pulsar Centaurus X-3. These observations of Cen X-3 were carried out with the *Rossi X-Ray Timing Explorer* (RXTE). The fluctuation spectrum is flat from millihertz to a few hertz, then steepens to f^{-2} behavior between a few hertz and ~ 100 Hz. Above 100 Hz, the spectrum shows the QPO features, plus a flat continuum extending to ~ 1200 Hz and then falling out to ~ 1800 Hz. These results, which required the co-adding three days of observations of Cen X-3, are at least as fast as the fastest known variations in X-ray emission from an accreting compact object (kilohertz QPO in LMXB sources) and probably faster since extension to ~ 1800 Hz is indicated by the most likely parameterization of the data. Multidimensional radiation hydrodynamics simulations of optically thick plasma flow onto the magnetic poles of an accreting neutron star show that the fluctuations at frequencies above 100 Hz are consistent with photon bubble turbulence and oscillations (PBO) previously predicted to be observable in this source. We show that previous observations of Cen X-3 constrain the models to depend on only one parameter, the size of the polar cap. For a polar cap opening angle of 0.25 radians (polar cap radius ~ 2.5 km and area ~ 20 km², for a neutron star radius of 10 km), we show that the spectral form above 100 Hz is reproduced by the simulations, including the frequencies of the QPO and the relative power in the QPO and the kilohertz continuum. This has resulted in the first model-dependent measurement of the polar cap size of an X-ray pulsar. The simulations underpredict the overall amplitude of the observed spectrum, which we suggest is the consequence of a two-dimensional axisymmetric simulation of an intrinsically three-dimensional phenomenon. The power-density spectrum of Cen X-3 shows a dramatic decrease above ~ 1000 Hz, which suggests an optical depth ~ 30 across the accretion mound consistent with effects of radiative diffusion in the simulations. We identify this decline at high frequency as the first direct evidence of radiative diffusion near the surface of a neutron star (NS). We suggest the fluctuations observed at frequencies below 100 Hz, whose spectrum has a different form from that of the kilohertz phenomena, reflect intermittency in the mass transfer mechanism that carries plasma from the accretion disk to field aligned flow onto the neutron star's polar caps. Using simple estimates based on Rayleigh-Taylor instabilities, possibly modulated by intrinsic disk turbulence, we show that mass transfer in “blobs” forming through Rayleigh-Taylor disruption of the disk's inner edge can explain the large amplitude fluctuations required by the spectrum at frequencies $f \sim 1$ Hz, but only if magnetic pressure in the disk's innermost regions inflates the disk until its scale height is comparable to the magnetosphere's size ~ 4300 km. The observational results required the development of a procedure for the careful determination of the dead-time effects of the PCA. This procedure is described in Appendix A. As a consequence of the use of observations of Cyg X-1 for the estimation of dead-time corrections for the observations of Cen X-3, we have also demonstrated that the black hole Cyg X-1 shows clear evidence of variability up to a frequency of ~ 280 Hz. Also observations of GX 17+2 were used to validate the procedure for dead-time corrections. This analysis of GX 17+2 clearly indicates the presence of a kilohertz QPO and the absence of any significant simultaneous kilohertz continuum.

Subject headings: instabilities — stars: individual (Cen X-3, Cyg X-1) — stars: neutron — stars: oscillations — turbulence

1. INTRODUCTION

The binary system composed of the X-ray-emitting neutron star Cen X-3 and its companion O-type supergiant has been studied extensively by all orbiting X-ray

astronomy observatories. The results from the *Uhuru* satellite identified the system as an eclipsing binary X-ray pulsar with a 2.087 day orbit and a 4.84 s pulse period (Giacconi et al. 1971; Schreier et al. 1972). The details of the orbit determination, which include estimates of the masses of both the neutron star and its companion, are summarized in a review (Rappaport & Joss 1983). The well-determined distance to the binary system (Hutchings et al. 1979) yields an accurate determination of the luminosity. Recently a cyclotron feature was detected in the X-ray spectrum of Cen X-3, providing precise knowledge of its surface magnetic field strength (Santangelo et al. 1998).

Table 1 summarizes the parameters of Cen X-3. The

¹ Space Sciences Laboratory, University of California, Berkeley, CA 94720; jgj@xnet.ssl.berkeley.edu.

² Department of Astronomy, 601 Campbell Hall, University of California, Berkeley, CA 94720; klein@radhydro.berkeley.edu, arons@astrophys.berkeley.edu.

³ Lawrence Livermore National Laboratory, University of California, L-23, P.O. Box 808, Livermore, CA 94550.

⁴ Department of Physics, University of California, Berkeley, CA 94720.

⁵ Theoretical Astrophysics Center, University of California, Berkeley, CA 94720.

TABLE 1
PARAMETERS OF CEN X-3

Parameter	Variable	Value	Lower Value	Upper Value	Reference
Mass of NS (M_{\odot})	M_{ns}	1.4	1.3	1.5	Rappaport & Joss 1983
Radius of NS (km)	R_{ns}	10.0	9.0	17.0	Baym & Pethick 1979
Cyclotron Line (keV)	E_c	28.5	27.5	29.5	Santangelo et al. 1998
Magnetic Field (Gauss)	B	3.2	3.1	3.3	Santangelo et al. 1998
Distance (kpc).....	D	10.0	9.0	11.0	Hutchings et al. 1979
X-ray Luminosity (10^{37} ergs s^{-1}).....	L_x	9.4	9.0	9.8	(this paper)
Polar Cap Radius (radians)	θ_c	0.25	0.1	0.4	(this paper)

average X-ray luminosity is

$$L_x = 9.4 \times 10^{37} \left(\frac{D}{10 \text{ kpc}} \right)^2 \left[\frac{(1+Z)}{1.3} \right]^2 \text{ ergs s}^{-1}, \quad (1)$$

where $Z = [(1 - 2GM/Rc^2)^{-1/2} - 1]$ is the surface gravitational redshift of the star of mass M and radius R . The surface magnetic field strength B implied by the observed cyclotron feature is

$$B = 3.2 \times 10^{12} \left(\frac{E_c}{28.5 \text{ keV}} \right) \left[\frac{(1+Z)}{1.3} \right] \text{ Gauss}, \quad (2)$$

where E_c is the energy of the cyclotron line. The measured mass of the neutron star combined with theory for the internal structure (Baym & Pethick 1979) constrains the range for its radius. If one assumes the magnetic field geometry at the surface to be dipolar, then the size of the polar cap onto which matter accretes is not well constrained by direct measurement.

Motivated by earlier predictions of the likelihood of the existence of photon bubble oscillations (PBO) in Cen X-3 (Klein et al. 1996a), we have analyzed two consecutive binary cycles of the source to search for PBO. We have also calculated new theoretical models constrained by the observable parameters of Cen X-3 (Table 1). The value for L_x is consistent with the observations reported here. The physics describing the radiation hydrodynamics that governs the accretion of matter onto the highly magnetized polar caps of luminous X-ray pulsars, and which has been incorporated in these new numerical simulations, has been described elsewhere (Arons, Klein, & Lea 1987; Klein & Arons 1989). Early numerical results (Klein & Arons 1991) and linear stability analysis (Arons 1992) suggested the formation of small-scale but large-amplitude fluctuations in the matter density and velocity, which form radiation filled pockets almost devoid of plasma (“photon bubbles”). These photon bubbles (PB) are embedded in the optically thick, inflowing plasma and as they grow nonlinearly, they result in significant observable fluctuations in the emitted luminosity.

We observed the X-ray emission from Cen X-3 with the *Rossi X-ray Timing Explorer* (RXTE) over two binary cycles of the source and clearly detect both kilohertz QPO and a broadband kilohertz continuum in the power-density spectrum that we identify with PBO and the high-frequency power-law continuum generated by photon bubble “turbulence.” (Our use of the descriptive noun turbulence should not be confused with the classical turbulence of a fluid.) Given the observationally derived physical parameters for Cen X-3 that are summarized in Table 1, the only remaining free parameter in our numerical models is the size of the polar cap. In this paper, we show that by adopt-

ing a reasonable size for the polar cap of Cen X-3, we are able to semiquantitatively match the frequencies of two observed QPO/PBO peaks and the kilohertz continuum with the power-density spectrum of our calculated radiation-hydrodynamic models; thus giving strong evidence for the existence of PBO and photon bubble turbulence in Cen X-3.

2. OBSERVATIONS

Separate continuous observations of Cen X-3 during 1997 February-March (JD 2450507.5067–JD 2450509.2248; JD 2450509.5470–JD 2450511.3304) were carried out with the PCA on-board *RXTE* (Bradt, Rothschild, & Swank 1993; Swank 1997) for two consecutive binary cycles of the source. Each observation lasted 1.7 days; during the non-eclipse phases of the binary orbit, data were acquired in two broadband energy channels at a time resolution of 62 μ s. The observation modes were specially selected to provide detailed information on the high time resolution behavior of the 4.8 s pulse as well as any broadband temporal behavior at frequencies above ~ 100 Hz. Figure 1 is a log-log presentation of the average dead-time corrected power-density spectrum for the entire data train of the low-energy channel (1–7 keV). The curve was computed by co-adding ~ 3400 separate power-density spectra, each with a ~ 65 s exposure and each composed of 2^{20} bins of duration 62 μ s. These power-density spectra were further averaged over frequency bins evenly spaced in logarithmic steps. This approach is the most sensitive way to search for broadband features in the power-density spectrum over a wide range of frequencies (10^{-2} to 10^4 Hz). Note the smooth plateau at very low frequencies (10^{-2} to 10^{-1} Hz) followed by the first and second harmonics of the 4.8 s pulse (10^{-1} to 10^0 Hz). The significance of the pulse is degraded by the crude averaging over frequency. However, the integral of the power density still correctly indicates the large pulsed fraction of the source. The periodic pulse and its harmonics are superimposed on a broadband power law that falls from an amplitude of $\sim 10^{-1}$ to 10^{-6} with a slope of approximately -2 (dashed line). At about 100 Hz another power-density plateau appears, followed by two QPO peaks (~ 331 and ~ 761 Hz). These two QPO peaks (50% confidence ranges 260–407 Hz and 671–849 Hz) are superimposed on the power-density plateau that falls sharply at frequencies above ~ 1200 Hz. The curve falls to a level of about $10^{-7}(\text{rms/mean})^2 \text{ Hz}^{-1}$ at ~ 1800 Hz that has reached the Poisson detection limit of the transform. The high-frequency Poisson limit in the form a frequency dependent function has been subtracted from the transform of the data (eq. [6] of Appendix A). The Leahy normalized version of the transform (Leahy et al. 1983) was carefully corrected for the effects of dead-time of the PCA (see Appendix A).

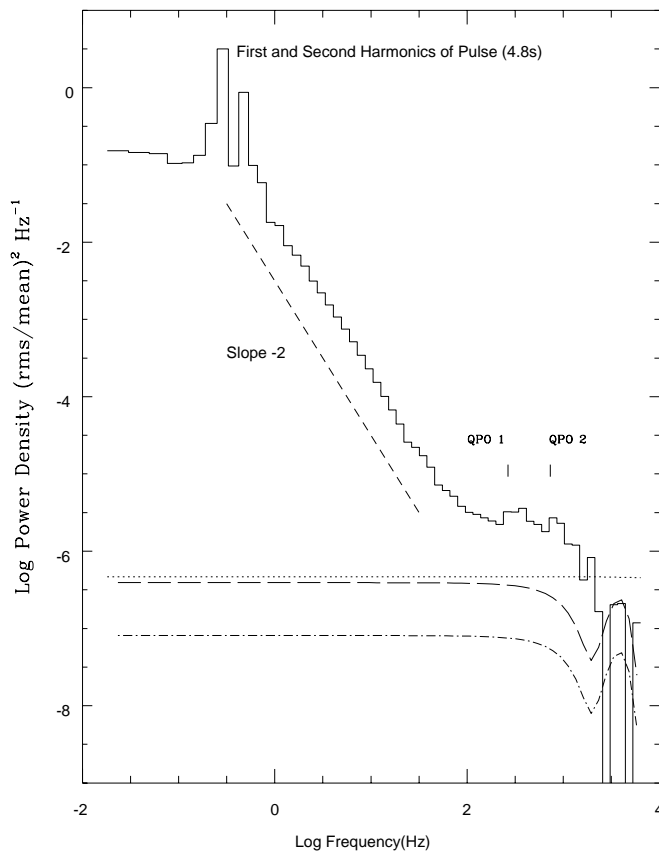


FIG. 1.—Curve is the observed average power density in units $\log_{10} [(rms/mean)Hz^{-1}]$ as a function of $\log_{10} [frequency (Hz)]$. Note the presence of the first and second harmonics of the pulse (0.21 and 0.42 Hz) due to the rotation of the neutron star, the power-law continuum below ~ 100 Hz with a slope of ~ -2 (dashed line), the flattening of the curve near 100 Hz, the two kHz QPO peaks, and the continuum power between 100–2500 Hz. This intrinsic power-density spectrum has been corrected for the effects of Poisson noise including the slight frequency dependence caused by dead-time effects of the PCA (see Appendix A). The dotted curve shows an estimate of the upper limit to the level of the dead-time corrected Poisson level. Power density at high frequency that falls below the dotted line is not confirmed as intrinsic to Cen X-3. The long-dashed curve just below the dotted curve shows the upper limit to any additive contribution from the background. This nonsource component of the power-density spectrum cannot be much larger than that shown here otherwise the peak at 4000 Hz would be detectable. The lower dot-dashed curve is the most likely level of the background based on the correction procedure (see Appendix A). The actual level of the background is likely another order of magnitude smaller than the dot-dashed curve.

The same analysis procedure was applied to the high-energy channel (> 7 keV). For these data the power-density spectrum is nearly identical to that shown in Figure 1 out to a frequency of about 50 Hz. We detect no significant kilohertz features. Determination of the energy dependence of the kilohertz features of the power-density spectrum must await significant additional PCA data or future detections with instruments of much larger aperture than *RXTE*.

We note that the identification of the specific features in the power-density spectrum as QPO in the presence of a significant continuum is a somewhat arbitrary description. Others may prefer to identify the QPO as “bumps” in the continuum or just as a complex continuum. In this paper, we choose to use the QPO designation in analogy with its use for the discovery of QPO in the LMXB source GX 5-1 (van der Klis et al. 1995a, 1995b). We justify this view based on the similar amplitude and width of these QPO in the

HMXB Cen X-3 and the low frequency (~ 6 Hz) QPO in the LMXB GX 5-1. Previous work on QPO in X-ray sources has indicated a large dynamic range of Q values including examples of order unity. The formal significance of the detection of these kilohertz QPO in Cen X-3 is not as high as for the QPO in GX 5-1 but this fact is likely just a coincidental result of the limited aperture of the PCA on-board *RXTE*. Even if these kilohertz features are real statistical fluctuations in behavior of Cen X-3, the QPO designation is still an appropriate description of the results presented in this paper. In using the QPO designation by observational analogy with GX 5-1 we do not suggest any underlying physical analogy.

A model composed of 15 free parameters was fitted to the power density over the frequency range 40–4000 Hz. These parameters are a low corner frequency F_l , a high corner frequency F_h , a level of power density P_l at the frequency F_l and its constant extension to lower frequencies, the slope S_l of a power law below the frequency F_l and its extension to higher frequencies, the slope S_m of a power law between the frequencies F_l and F_h , the slope S_h of a power law above the frequency F_h and its extension to higher frequencies, the frequency of the first Gaussian QPO F_1 , its rms amplitude A_1 and its width W_1 , and the frequency of the second Gaussian QPO F_2 , its rms amplitude A_2 and its width W_2 . Finally, the last three parameters (A, B, and C) model the frequency dependent dead-time correction to the power-density spectrum (see Appendix A for details).

Alternative forms of the continuum power density will slightly change the values of the six parameters that describe the two QPO peaks but will not change the basic interpretation of the fit. This particular functional form for this model was selected as a reasonable choice for a simple characterization of the full power-density spectrum between 40–4000 Hz with particular attention to the frequency range ~ 100 –2000 Hz.

Table 2 displays a list of the parameters and their best fitted values, as determined by a minimization of χ^2 . The errors in the measured power-density points were determined by the Poisson counting noise. These data are comprised of 39 independent points, resulting in a minimum χ^2 per degree of freedom of 1.38 for 24 degrees of freedom. Formally this is not an adequate fit; however, inspection of the residuals indicates that the fit is within expected limits for frequencies between 100–2000 Hz (see Fig. 9 in Appendix A).

All components of the model match the data well except for small deviations at low frequencies (see Figs. 2 and 9). The minor deviations from a power law at low frequencies (< 100 Hz) are revealed by the extremely small error bars. These deviations that are a small fraction of the power density at low frequency are likely caused by a real physical mechanism that is more complex than a simple power law. Since the primary goal of this paper is to characterize the kilohertz behavior of Cen X-3 we did not further complicate the fifteen parameter model. The high-frequency data are of insufficient signal to noise to realistically determine the exact nature of this detailed structure in the falling power density. The uncertainty in the interpretation of the decline in power above ~ 1200 Hz is quantified by the large acceptable range of the parameter S_h . The presence of the two QPO peaks and the broadband kilohertz continuum in the power spectrum over the frequency range 100–1800 Hz is highly significant. Setting the amplitudes of the QPO peaks

TABLE 2
FITTED MODEL PARAMETERS

Parameter	Variable	Value	Lower Value	Upper Value	Units
Low Corner Frequency	F_l	63	46	76	Hz
High Corner Frequency	F_h	1228	923	1662	Hz
PD(F_l)	P_l	2.50	2.05	2.95	$10^{-6} (\text{rms}/\text{mean})^2 \text{ Hz}^{-1}$
Low PD Slope	S_l	-2.15	-3.89	-1.04	dimensionless
Mid PD Slope	S_m	-0.27	-0.37	-0.18	dimensionless
High PD Slope	S_h	-2.61	-8.1	-1.5	dimensionless
Frequency of QPO 1	F_1	331	260	407	Hz
Amplitude of QPO 1	A_1	3.1	2.1	3.9	percent rms
EW of QPO 1	A_1	712	329	1106	Hz
Width of QPO 1 (1σ)	W_1	89	48	213	Hz
Width of QPO 1 (FWHM).....	W_1	214	115	511	Hz
Q of QPO 1 (FWHM).....	F_1/W_1	1.5	1.2	1.9	dimensionless
Frequency of QPO 2	F_2	761	671	849	Hz
Amplitude of QPO 2	A_2	3.1	2.0	4.0	percent rms
EW of QPO 2	A_2	969	426	1534	Hz
Width of QPO 2 (1σ)	W_2	103	36	262	Hz
Width of QPO 2 (FWHM).....	W_2	247	86	629	Hz
Q of QPO 2 (FWHM).....	F_2/W_2	3.1	2.7	3.4	dimensionless
Dead-time Factor	A	0.01304	0.01285	0.01328	dimensionless
VLE Dead-time Factor	B	0.00071	0.00048	0.00095	dimensionless
Background	C	0.00011	-0.00032	0.00055	dimensionless

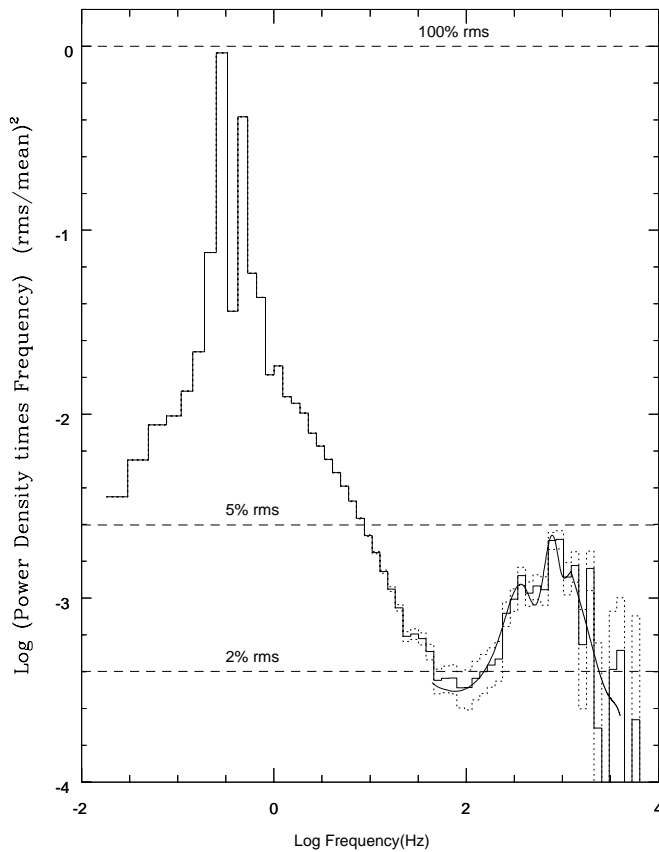


FIG. 2.—Curve of measured data (solid stair step) is the same as in Fig. 1, but has now been multiplied by frequency. Dotted lines are plotted above and below the data at 1σ error levels. Dashed lines are plotted horizontally at levels of 1%, 5%, and 100% (rms/mean). Note that the pulsed fraction is at a level of several tens of percent. The two kHz QPO peaks and the continuum power above 100 Hz have a total power bounded between 1% and 5% rms. The best fit to the data plotted as a continuous solid curve tracks the measurements.

to zero results in an increase in χ^2 of ~ 47 and ~ 42 for QPO 1 and QPO 2, respectively. This implies that the first and second QPO peaks are formally detected at greater than 99.9% confidence. The lower and upper values of the parameters in Table 2 are 50% confidence limits for each of the fifteen free parameters of the model. (These are determined by the variation of each parameter until χ^2 increased by ~ 14.34 ; see Lampton, Margon, & Bowyer 1976.)

The form of the fitted model for the low-frequency (40–100 Hz) power law was selected with the assumption that whatever the physical mechanism that forms this power law that behavior is likely to continue past 100 Hz. Since the extrapolation of the low-frequency power law above 100 Hz is much lower than the observed power density in the kilohertz band this suggests a transition near 100 Hz in which a new physical mechanism becomes dominant. Note that the continuation of the power law to very low frequency (< 3 Hz) rolls over to a flat level as required by causality since this extrapolation cannot produce fluctuations that exceed 100% rms. This damping of the behavior at low frequency is still consistent with a single physical mechanism. Possibilities for the physics that generates this low-frequency power law are discussed in a later section.

Figure 2 shows the dead-time corrected data with $\pm 1 \sigma$ error bars (dotted lines) as well as the model (solid line). The data have been multiplied by frequency in order to more clearly indicate the Poisson counting noise. This also means that the vertical axis has units of $(\text{rms}/\text{mean})^2$, which allows for the easy approximate interpretation of features in units of rms percentage amplitude. Dashed horizontal lines at 2%, 5%, and 100% are shown to indicate the relative amplitudes of features of the power-density spectrum. The coherent pulsations from Cen X-3 clearly have a large amplitude of order $\sim 50\%$ whereas the high-frequency components (> 100 Hz) have amplitudes in the 2%–5% range. The best fitted fifteen parameter model is also plotted in Figure 2 and

clearly tracks the measured data. Note the presence of the two kilohertz QPO peaks (~ 330 Hz and ~ 760 Hz) and the break in the continuum at the high corner frequency ($F_h \sim 1200$ Hz).

3. THEORETICAL MODEL

Photon bubble instabilities can form in magnetized radiation pressure supported atmospheres and subsonic flows (Klein & Arons 1989; Arons 1992) with B fields as small as 10^8 Gauss. Classical X-ray pulsars such as Cen X-3 easily fulfill this criterion. We calculate a model appropriate for the surface conditions of the neutron star Cen X-3. This model relies on the self-consistent solution of the full two-dimensional, time-dependent equations of the radiation hydrodynamics governing the accretion of matter onto the highly magnetized polar caps of a luminous X-ray pulsar (Arons et al. 1987; Klein & Arons 1989; Klein et al. 1996a). The full description of the physics of highly magnetized flow that we have included in our calculations is described in detail in Arons et al. 1987. We solve the full set of two-dimensional, time-dependent relativistic radiation hydrodynamic equations. These include the equations which govern the conservation of mass and momentum, and separate energy equations for both the electrons and the ions as well as a full non-LTE description of the time dependent transport of radiation and photon number density (Klein & Arons 1991). We also include the full effects of super strong magnetic fields on all physical processes and we have developed a new flux-limited diffusion theory for the transfer of radiation in optically thin, radiation filled structures embedded in optically thick flows (photon bubbles). We solve the entire structure of self-consistent two-dimensional coupled nonlinear PDEs with a second-order accurate, time explicit operator splitting approach.

The full evolution of the radiation hydrodynamic equations is an initial value problem in time. The surface value of the magnetic field strength assumed to have dipole geometry, the mass accretion rate, and the size of the polar cap are all parameters, as are the mass and radius (which enter into the strength of gravity) of the neutron star. We hold these characteristics fixed in the course of a calculation (see Table 1 for values). This leaves the geometry of the polar cap as the only free parameter in the calculation. In principle, a specification of the surface field strength B_0 and the intrinsic luminosity L_X could, under certain assumptions (i.e., magnetic dipole field configuration) determine the radius of the polar cap θ_c (Pringle & Rees 1972; Davidson & Ostriker 1973; Lamb, Pethick, & Pines 1973; Arons & Lea 1980). The details of the magnetospheric mass loading are quite uncertain. Since these details determine the size of the polar cap and the distribution of the accretion mass flux within the polar flux tube, we simplify by assuming the accretion flux to be constant from the magnetic axis out to a fixed magnetic flux surface, then zero beyond, and we take the polar cap radius to be the only free parameter in our calculations.

From our previous calculations with $L_X = 3 \times 10^{37}$ ergs s^{-1} and $B = 3 \times 10^{12}$ G, we know that in models with large polar caps ($\theta_c = 0.4$) we obtain two PBOs with frequencies of 170 Hz and 260 Hz (Klein et al. 1996b), while smaller polar caps ($\theta_c = 0.1$) yield PBO with significantly higher frequencies in the range of 3500 Hz (Klein et al. 1996a). Thus wider accretion columns produce PBO of lower fre-

quency, a scaling most likely related to the longer diffusion time necessary for photons that originate in interior photon bubbles of wider columns to diffuse to the outer edge of the accretion column. Therefore, PBO at the observed frequencies at 330 and 760 Hz should occur for polar cap sizes bounded by our previous calculations, $0.1 < \theta_c < 0.4$. We have computed three new models to explore the variation of PBO frequency with polar cap sizes $\theta_c = 0.25, 0.3$ and 0.4 , with the luminosity $L_X = 4.7 \times 10^{37}$ ergs s^{-1} and magnetic field strength $B = 3.2 \times 10^{12}$ G inferred from observations of Cen X-3. The value of L_X selected here is one half of that shown in Table 1 that is appropriate for one of the two polar caps. The calculations refer to accretion onto a single polar cap.

Since the basic oscillation and instability timescales of the magnetically modified g -modes that become photon bubbles are proportional to the timescale for radiation diffusion (Arons 1992), and photon escape from the sides of the column controls the emergent intensity, one can reasonably suppose that the timescale for radiation diffusion across the magnetic field, $t_{\text{diff}} \simeq L_{\perp}^2(3/c\lambda_{mf,p,\perp}) = L_{\perp}/V_{\text{diff}\perp} \propto \theta_c^2$, might be related to PBO timescales. This strong dependence on θ_c is amply supported by the simulations previously published and reported here. Here $V_{\text{diff}\perp} = c/3\tau_{\perp}$ is the diffusion velocity across the flow above the accretion shock, with τ_{\perp} the scattering optical depth across the magnetic field. L_{\perp} is the transverse distance across the magnetic field, which at the base of the accretion mound on the stellar surface is $R_* \theta_c$, but further up in the accretion column is $R_* \theta_c (r/R_*)^{1.5}$. The parameter $\lambda_{mf,p,\perp}$ is the transverse mean free path across the accretion mound. We find in the $\theta_c = 0.25$ model that just above the accretion shock at the accretion mound, $\tau_{\perp} = 19$ and $L_{\perp} = 6 \times 10^5$ cm, yielding $t_{\text{diff}} = 1.14 \times 10^{-3}$ s. This corresponds to a diffusion frequency $\nu_{\text{diff}} = 877$ Hz. At the base of the accretion column, we find $\tau_{\perp} = 80$ yielding $t_{\text{diff}} = 2 \times 10^{-3}$ s and the corresponding diffusion frequency $\nu_{\text{diff}} = 500$ Hz.

Calculating the transverse radiation transport speed as F_{\perp}/E_{rad} at the accretion shock, where F_{\perp} is the transverse radiation flux and E_{rad} is the radiation energy density in the $\theta_c = 0.25$ model, and setting the result equal to V_{diff} gives a diffusion speed of 1.0×10^9 cm s^{-1} and a diffusion time $t_{\text{diff}} = 6.04 \times 10^{-4}$ s. This corresponds to a diffusion frequency $\nu_{\text{diff}} = 1.6 \times 10^3$ Hz. Taking the measurement of the transverse radiation transport speed near the base of the accretion column gives $V_{\text{diff}} = 5 \times 10^8$ cm s^{-1} , $t_{\text{diff}} = 5 \times 10^{-4}$ s and $\nu_{\text{diff}} = 2000$ Hz. Thus the two ways of computing the diffusion time are in agreement within roughly a factor of 2. Considering these approximations, one might expect this model to show PBO with fundamental frequency $\nu_{\text{PBO}} \sim 1000$ Hz, not drastically different from the values found in the computational model and in the observations of Cen X-3. The uncertainty in the quantification of the diffusion time to within a factor of 2 is a consequence of the highly nonuniform structure of the accretion column. If the column were uniformly dense, the two approximations for τ_{diff} would be in more precise agreement. This factor of 2 uncertainty has no bearing on the accuracy of the PBO centroid frequencies which are determined by the solutions of the full radiation hydrodynamics equations in a spatially inhomogeneous medium. Thus the final PBO centroid frequencies represent a complex path for photons through intermingled optically thick and thin plasma. A diffusion time estimated at a few points in such a medium is not likely

to be better than a factor of 2 in accuracy. A Monte Carlo treatment following the time history of the photons in the accretion column would be necessary to get a precise determination of the diffusion time for photons to leak out of the column.

We identify the high corner frequency ~ 1200 Hz noted previously with an average diffusion timescale t_{diff} which we relate to the total optical depth τ_{obs} across the accretion mound.

$$\tau_{\text{obs}} = 26 \left\{ \left(\frac{F_h}{1200 \text{ Hz}} \right) \left[\frac{(1+Z)}{1.3} \right] \right\}^{-1} \times \left(\frac{\theta_c}{0.25 \text{ radians}} \right)^{-1}, \left(\frac{R_*}{10 \text{ km}} \right) \quad (3)$$

This equation for τ_{obs} is a recasting of the expression for the diffusion time t_{diff} , now expressed in terms of the optical depth. The form of equation (3) indicates how the value of τ_{obs} varies depending on the assumed size of the polar cap, θ_c . The particular value of θ_c is the assumed value that we used for model A, which also corresponds to a typical value within the expected range for θ_c (see Table 1). Basically, any internal oscillations within the interior of the accretion mound that are faster than the high corner frequency are suppressed by a factor that scales approximately as the inverse second power of frequency. This simple scaling is the result of the approximation that diffusion is just a smoothing process by a linear filter with a characteristic timescale. The estimated value of the optical depth $\tau_{\text{obs}} \sim 26$ agrees approximately with the values of optical depth in the numerical calculations (typically ~ 20 – 80). This agreement is not expected to be better than a factor of a few because of the simplifying assumption of a uniform medium with a diffusion velocity ($c/3\tau_{\text{obs}}$). We identify this feature at high frequency as the first direct evidence of radiative diffusion near the surface of a neutron star (NS).

4. RESULTS OF RADIATION HYDRODYNAMIC CALCULATIONS

Figure 3 shows the results for the power-density spectra of the time series of the emergent transverse luminosity out of the sides of the accretion column for three models (A, B, and C) for which the values L_x and B have been set to those measured for Cen X-3 (see Table 1). The models A, B, and C are distinguished by setting the polar cap size to 0.25, 0.3, and 0.4 radians respectively. The power-density spectrum for each model is obtained by first performing a full two-dimensional time-dependent radiation-hydrodynamic calculation and obtaining the radiative flux in the transverse direction. This flux is integrated along a series of annular rings along the sides of the accretion funnel to obtain the emergent luminosity, which exits the accretion column in a low-altitude fan beam of radiation. The time series of the transverse luminosity is then Fourier transformed to obtain the power-density spectrum.

These models are simulations of only a few tens of milliseconds of accretion onto the neutron star and may not be well defined ergodic samples necessary for an exact comparison with the observed power-density spectra averaged over many thousands of seconds. However, in support of making such comparisons of simulations to observations, we point out that any initial transients in the calculations die out after less than 10% of the running time for each

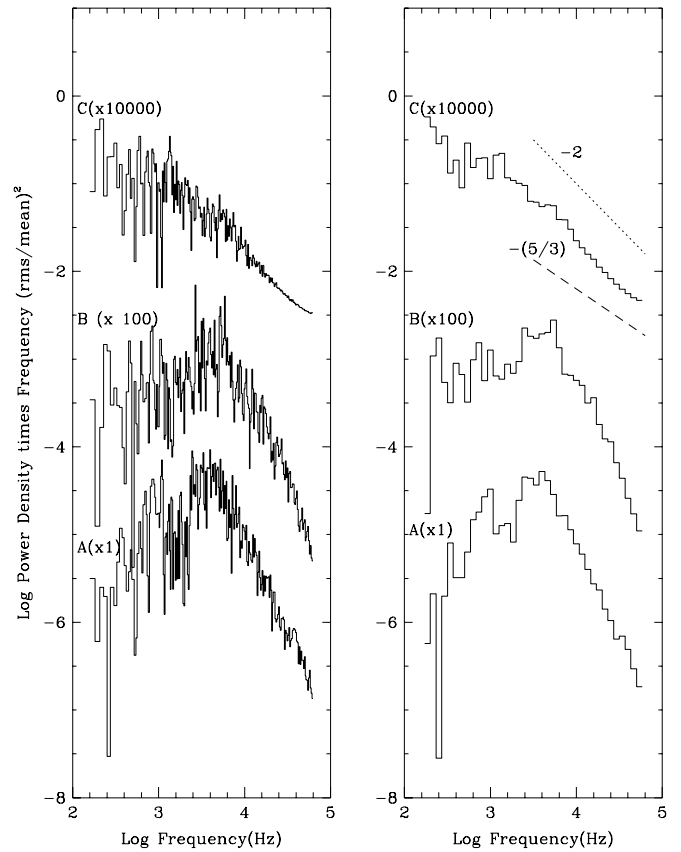


FIG. 3.—Left panel is a log-log plot of power-density spectra in units \log_{10} [power density(rms/mean)] of models A, B, and C vs. \log_{10} [frequency (Hz)]. The right panel is a smoothed representation of the data in the left panel and is more appropriate for direct comparison with the observed data. The vertical scale has been shifted up by 2 and 4 decades for models B and C respectively for illustrative purposes. Note that all three models show evidence of PBOs and PB continuum power. Lines that indicate power laws of the form f^{-2} (dotted) and $f^{-(5/3)}$ (dashed) are indicated in the right panel. These slopes at high frequency are roughly consistent with the results that we reported previously (Klein et al. 1996b).

simulation. The power spectra calculated from the simulations are derived from the remaining $\sim 90\%$ of each run, corresponding to what appears to be a statistically steady state. Our procedure limits the quality factor, Q , of any individual PBO to the ratio of the simulation's length to a given PBO period ($Q < 100$). Our procedure obviously would miss slow changes of the apparent statistically steady states observed. We have no reason to believe that there are such slow systematic effects, given the physics incorporated in the simulations. Therefore, we take the simulations as our best known estimates of the behavior of PBO over times much longer than characteristic PBO periods. We further note that the errors on the actual calculation of the power densities are very small (less than 10^{-8}) in the units shown in Figure 3. The detailed features in the power densities are formally *very* significant with none of the degradation at high frequencies that typify observations containing Poisson counting noise. These very small errors, which cannot practically be shown in Figure 3, are due to the finite spatial grid and discrete time steps of the numerical calculations. This level of this numerical noise in the power density is revealed by an artificial downturn at very high frequencies ($\sim 10^5$ Hz). Typically, time steps in the calculations are $\leq 5 \times 10^{-5}/\nu_{\text{PBO}}$.

In Figure 3 the lower curve is model A ($\theta_c = 0.25$ radians), the middle curve is model B ($\theta_c = 0.3$ radians), and the upper curve is model C ($\theta_c = 0.4$ radians). Models B and C have been artificially shifted by two and four decades vertically for illustrative purposes. The curves in the left panel are shown in high resolution to reveal the details of structure of the power-density spectrum. Below a frequency of ~ 1 kilohertz the spectrum is shown at the full resolution of the calculations. At higher frequencies the data are smoothed in equal logarithmic intervals for clarity of presentation. The curves in the right panel show the same data further smoothed to facilitate comparison with observations (see Fig. 2) and to enhance the broadband features. The most striking common feature of all three models is the roll-off at high frequencies in approximate agreement with equation (3) and a clear demonstration of the signature of radiative diffusion. In detail Models A and B show a somewhat steeper slope at higher frequencies, which is not as likely considering the rough approximation of equation (3). Each curve has a principal low-frequency PBO that is shifted to higher frequency for the models with smaller polar caps in good agreement with $\nu_{\text{PBO}} \propto 1/\theta_c^2$ scaling. The lower frequency PBO in model A determined from the detailed calculations is ~ 350 Hz (not redshifted), which agrees well with the observed lower frequency QPO for Cen X-3 (~ 330 Hz). Our detailed calculations yield lower frequency PBO approximately at 250 Hz and 200 Hz for models B and C with $\theta_c = 0.30$ radians and $\theta_c = 0.40$ radians, respectively. These are in reasonable agreement with the frequencies 246 Hz and 138 Hz suggested by θ_c^2 scaling. Also the level of the continuum is somewhat lower for models with smaller polar caps.

Note that the absolute levels of the power density can be directly compared to the observed levels in Cen X-3 (see Fig. 2). The amplitude of the observed power density in the range 100–1800 Hz is about 1 or 2 orders of magnitude higher than the level calculated in the theoretical models. This discrepancy is not that severe considering the simplified model for the geometry of the emission region. The actual rms amplitudes of the fluctuations in the models near 1 kilohertz are only a factor of 10 lower than the observed level. The variability of the escaping X-ray luminosity is a damped form of the more violent internal photon bubble variability deep within the accretion mound. The presence of the PBs within the mound necessarily implies the local internal opacity variations have rms amplitudes that reach nearly 100%. In an extension of the two-dimensional theoretical models to three-dimensional we would expect the variations of opacities “seen” by internally generated photons to vary by an even wider range. Some of these photons might “see” reduced opacities episodically, which would significantly enhance the X-ray variability and rms amplitudes seen by a distant observer. Also the assumption of a uniformly filled accretion column might be relaxed as a partially filled column (hollow cone) would also provide lower opacity paths from the interior of the shock mound to the exterior surroundings. We are extending our calculations to a hollow cone accretion geometry as the first step toward investigating three-dimensional effects on the amplitude of the PBO fluctuations. This work will be reported elsewhere. There are likely very low-frequency variations (< 1 s or pulsed modulated at 4.8 s) in the geometry of the matter filling the accretion column that would result in low-opacity “windows” that would allow a distant observer to

“see” into the interior of the shock mound where the rms fluctuations of the X-ray emission are much higher.

Model A ($\theta_c = 0.25$ radians) shows PBO at 350 Hz and a composite PBO at about 700 Hz. The frequencies of these PBO are in good agreement with frequencies of the QPO peaks observed in the power-density spectrum of Cen X-3. The relative amplitudes of the PBO/QPO as compared to the continuum power are a better match between the theory and observation than the absolute amplitudes. The rms amplitudes of the observed QPO 1 and 2 in Table 2 can be expressed as equivalent widths (~ 710 Hz and ~ 970 Hz) that are comparable to the full range of the continuum (~ 100 Hz to ~ 1800 Hz) indicating an approximately equal contribution of the QPOs and the continuum to the full rms amplitude above ~ 100 Hz. The approximate balance between PBO/QPOs and continuum is also roughly true for all three theoretical models. The additional strong broad composite PBO at ~ 3000 Hz that is seen in models A and B is not seen in the observed power-density spectrum of Cen X-3. However it is below the level that could be easily detected with the PCA. The upper limit for the detection of broad features in the power-density spectrum rises proportional to frequency above ~ 1000 Hz, which rapidly decreases the capability for detection of any features near 3000 Hz. This rapidly declining ability to detect broad features at high frequencies should not be confused with the flat asymptotic behavior for the detection of features of fixed bandwidth that have increasing Q -values at higher frequencies.

Models A, B, and C have been plotted simultaneously with the observed data in Figure 4. For comparison both models and the observed data have been plotted over an appropriate frequency range and on the same absolute scale with no effort to adjust the amplitudes to match the data. The frequencies of the theoretical simulations have been red-shifted correctly by the required factor of $(1 + Z) = 1.3$ appropriate for the surface of a neutron star with mass and radius specified in Table 1. The frequencies of the PBO in model A match the frequencies of the QPO in the observed data. This is remarkable considering that the only free parameter in our calculations is the size of the polar cap. The theoretically determined PBO at ~ 300 Hz and the corresponding observed QPO at a similar frequency are both relatively weak in comparison to the PBO/QPO at ~ 700 Hz. In addition model A (also B) has a broad PBO with a large amplitude at ~ 3000 Hz that is very near the limit of the observable range of *RXTE* (Fig. 3). The continuum shape of model A does not match the observations as well as model C (Fig. 4). All three models show a power law roll-off at high frequency ($\sim 10^4$ Hz) in agreement with the simple approximation that diffusion is just a smoothing process by a linear filter with behavior f^{-2} . Models A and B show a somewhat faster roll-off at even higher frequencies. If we consider the whole picture, model A has the best QPO/PBO frequency match and models B or C have a better match to the continuum. These models taken together determine a range for the polar cap radius of ~ 2 – 3 km. Calculations are underway (to be reported elsewhere) to better bracket the polar cap radius by doing a parameter study of small variation of the polar cap radius around our best model A with $\theta_c = 0.25$ radians, and its effect on the PBO frequencies. These calculations are extremely time consuming and typically require ~ 300 hr per model on a supercomputer.

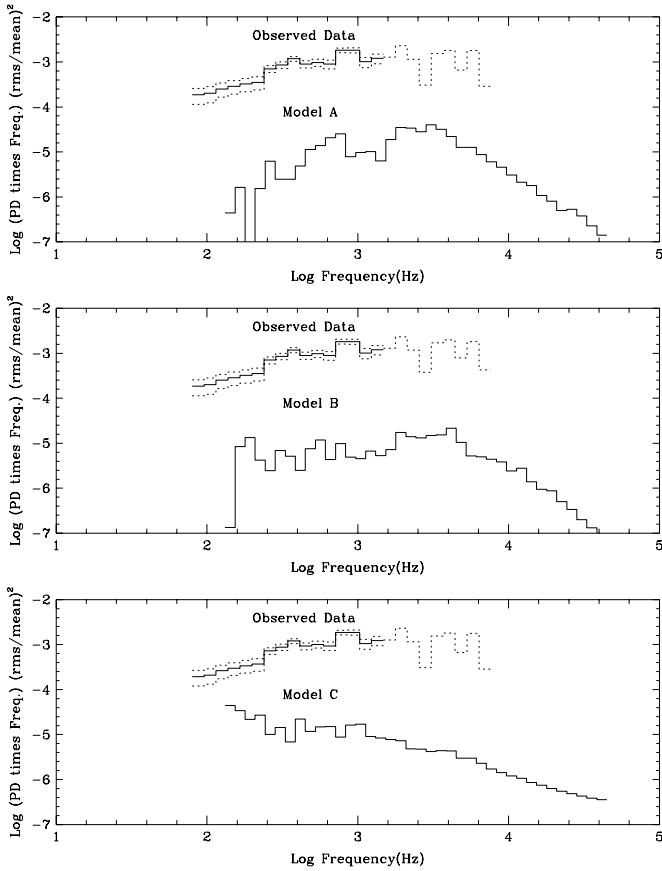


FIG. 4.—Upper curve in each panel is the observed power density of Cen X-3 from Fig. 2. The error bars are shown to facilitate a quantitative comparison to the theoretical models. Beyond ~ 1800 Hz the 2σ upper limit is shown as a dotted curve. Also the low-frequency power law fitted to the observed data has been subtracted since this component of the observed spectrum is not included in the physics incorporated into the theoretical models. The power-density spectra of the three models A, B, and C are shown on the same absolute scale. These are the smoothed versions of the spectra appropriate for direct comparison to the observed spectrum of Cen X-3. The three models have been correctly red shifted by the appropriate amount for the surface of a neutron star.

Our calculations have used measured parameters for Cen X-3 (e.g., luminosity, magnetic field, mass, etc.) while only varying the size of the polar cap. Hence the identification of the kilohertz QPOs and a kilohertz broadband continuum with PB phenomena suggests that the radius of the polar cap of Cen X-3 is “measured” as ~ 2 – 3 km. This is the first, albeit model dependent, measurement of the size of the accreting polar cap of an X-ray pulsar.

5. DISCUSSION OF LOW-FREQUENCY BEHAVIOR (< 100 Hz)

A simple power law with a slope ~ -2 matches the broadband continuum from 3–100 Hz in the power-density spectrum of Cen X-3 (see Figs. 1 and 2 and Table 2). This general behavior has been previously reported for Cen X-3 and other HMXB sources (Belloni & Hasinger 1990).

The origin of this lower frequency noise may be the consequence of the physics controlling the loading of mass onto the magnetospheric field, perhaps modulated by intrinsic turbulence in the disk. In the case of Cen X-3, the mass flow exterior to the magnetosphere is almost certainly in an accretion disk. To fix ideas, suppose the boundary layer between the disk and the magnetosphere is Rayleigh-Taylor unstable, a mass entry mechanism previously treated in

some detail for the case of spherical accretion by Arons & Lea (1976, 1980 and Elsner & Lamb (1977, 1984). Some aspects of Rayleigh-Taylor instability in the disk/magnetosphere interaction have also been discussed by Taam & Spruit 1990.

The thickness and height $H = R_m(c_{ms}/v_K)$ of the disk’s boundary layer set the size of an unstable mode (a “blob”). Then $\delta M \sim \rho H^3$ is the mass of a blob, while in statistically steady accretion $\rho = \dot{M}/2\pi HR_m v_K$ (see Arons 1993 for this result, in the relevant case when the plasma is diamagnetic, and Ghosh & Lamb 1979 when macroscopic dissipation is assumed to give the free access of the neutron star’s magnetic field to the disk’s plasma on microscopic scales.) Here $R_m \approx 4300$ km is the magnetopause radius, evaluated assuming approximate corotation between the Keplerian disk’s inner edge and the magnetosphere (Bildsten et al. 1997), $v_K \approx 5580$ km s $^{-1}$ is the Kepler velocity of the disk just outside the magnetopause, and $c_{ms} = (c_s^2 + v_A^2)^{1/2}$ is the magnetosonic speed in the disk, with c_s the sound speed and v_A the Alfvén speed determined by the disk’s own magnetic field. Compton scattering of the hard X-rays from the star limits the sound speed to $c_s \sim 1000$ km s $^{-1}$. As we shall show, in mass transfer by blobs, the disk’s inner edge must have a strong magnetic field of its own, such that $v_A^2 \gg c_s^2$.

The mass of a blob is $\delta M = \rho H^3 \sim \dot{M} H^2 / 2\pi R_m v_K$, and the number of blobs contributing to the mass flow is $N_{\text{blob}} \approx 2\pi R_m / H$. Therefore, in a statistically steady state,

$$\dot{M} = \frac{d}{dt} N_{\text{blob}} \delta M \sim \frac{N_{\text{blob}} \delta M}{\tau t_{ff}} = \frac{\sqrt{2}}{\tau} \dot{M} \frac{H}{R_m}. \quad (4)$$

Here τ is the number of magnetospheric free fall times $t_{ff} = R_m/v_{\text{ff}}(R_m) = (R_m^3/2GM_*)^{1/2} \sim 0.46$ s required for a blob to form, decelerate, and freely fall through a distance $\sim H$, thus detaching from the boundary layer. This detachment process is very ill understood. If one assumes the blob loses its orbital velocity instantaneously, then $\tau = 4$ ($H/R_m \ll 1$), while $\tau \approx 3$ if $H/R_m \sim 1$. τ is expected to be larger still, if one accounts for the mechanical and electromagnetic drag forces on the forming blob.

Eliminating \dot{M} from 4 yields

$$\frac{H}{R_m} = \frac{c_{ms}}{v_K} \approx \frac{\tau}{\sqrt{2}} \approx \frac{3}{\sqrt{2}} \sim 2. \quad (5)$$

Therefore, the inner edge of the disk must be reasonably thick, with $N_{\text{blob}} \sim 2\sqrt{2}\pi/\tau \sim 3$ blobs contributing at any one time to the mass flow, and the magnetic pressure in the disk must be large compared to the gas pressure. For Cen X-3’s parameters, we find $B^2/4\pi \sim 230nkT_{\text{gas}}$. Note that we have neglected the inflationary effects of radiation pressure on the disk. Since Cen X-3’s luminosity is $\sim 30\%$ of the Eddington luminosity, some of the disk’s inflation might be supported radiatively rather than magnetically, but it is hard to avoid the conclusion that magnetic support makes a large and probably dominant contribution to the disk’s inner structure.

Such variability in the accretion flow will cause the size of the polar cap to vary. In the “kinematic” estimates of the size of the polar cap as a function of \dot{M} (Pringle & Rees 1972; Davidson & Ostriker 1973; Lamb et al. 1973), $\theta_c \propto (R_*/R_m)^{1/2} \propto \dot{M}^{1/7}$. Such a model might apply if (1) macroscopic reconnection causes all dipole field lines that would have closed at radii $r > R_m$ to be open and (2) blobs do not fall to radii substantially smaller than R_m before their par-

ticles become frozen to magnetospheric field lines. If, on the other hand, blobs form diamagnetically, lose their angular momentum and fall freely before disrupting into particles that freeze to the magnetospheric field, then $\theta_c \propto M^{-2/7}$ (Arons & Lea 1980). If blob formation causes the mass flux onto one pole to vary by as much as $[1/(N_{\text{blob}}/2)]^{1/2}$, then in Cen X-3, the polar cap size might be varying by as much as 12% (open field model) or 23% (freely falling blob model) over the course of the 3 days of observation that went into forming the power spectrum. In principle, we should compare the average of several models similar to model A but with different values of θ_c to the high-frequency fluctuation power, rather than the single “snapshots” shown in models A, B, and C. However, the expected small range of variation in θ_c suggests the snapshot comparison to be good enough, given the limitations in the simulations.

Consideration of Kelvin-Helmholtz (KH) mixing (e.g., Burnard, Lea, & Arons 1983); lead to similar conclusions. The KH effects most likely contribute to blob formation and deceleration, while Rayleigh-Taylor (RT) instabilities control the detachment of blobs from the disk’s inner edge. For both effects, the basic mode size is H , and the mass transfer rate is controlled by gravitational free fall, so our order of magnitude estimates are invariant to the greater complexity of considering both RT and KH together. On the other hand, if the mass transfer were to be controlled solely by reconnection, with a mass loading velocity $\sim \epsilon v_A$ with ϵ perhaps on the order of 0.1 (see Lazarian & Vishniac 1999 for a recent investigation of rapid reconnection and full references on the subject). Repetition of our arguments lead to $H/R_m \sim 2\pi/\epsilon \gg 1$, which is impossible since the magnetic stresses would cause the disk to explode and shut off accretion.

These estimates lead to several important conclusions. Only $N_{\text{blob}} \sim 3$ “blobs” contribute to the mass flow onto each polar cap at one time, with the basic timescale for these slow fluctuations being $\tau_{\text{ff}} \sim 1.4$ s. Thus, the observed fact that spectrum flattens at less than 3 Hz can be understood as the consequence of the fluctuations becoming large amplitude at these low frequencies. Possibly additional fluctuations are imposed on the structure of the blobs by intrinsic disk turbulence. Hawley has calculated models of disk turbulence that show a scale free power-law dependence of the spatial transform of density, velocity, and kinetic energy of the flow (Hawley, Gammie, & Balbus 1995). The necessary truncation of the power law on the largest scale corresponds to overturning velocity structure of order the inner disk scale height. These slowest components of the flow could naturally explain the flattening of the temporal transform at low frequency (< 3 Hz). The power law form of the spatial transform would naturally imply a power law form of the temporal transform. The reality of these fluctuations depends on the assumption that the disk variability imposes a structure on the formation of blobs. Further, since the Rayleigh-Taylor modes can include structure elongated along the circumference of the magnetosphere (“blob” azimuthal lengths between $\sim H$ and $\sim 2\pi R_m$), lower frequency power might also be caused by modulations of the flow due to azimuthal structure in the instabilities, especially if one takes account of the time needed to get rid of the orbital velocity and allow a blob to go into free fall. Quantitative consideration of these more advanced issues is far beyond the scope of this paper. However, whatever mechanism modulates the accretion rate and accounts for the low-

frequency (3–100 Hz) power law with a slope ~ -2 , its behavior is likely to extrapolate as a continuation of the same power law to higher frequency (> 100 Hz). Therefore the deviation from this power law at greater than 100 Hz that is observed in Cen X-3 is likely a different physical mechanism associated with the surface of the neutron star.

6. CONCLUSIONS

We have advanced the view that the fluctuations observed in the power spectrum at frequencies exceeding a few hundred Hz have their origin in the intrinsic photon bubble instability of the accretion flow at the stellar surface, rather than being the passive result of still higher frequency fluctuations in the mass loading into the magnetosphere. Empirically, this view is supported by the change in the power spectrum’s structure above a few hundred Hz. From the point of view of polar cap plasma dynamics, the large amplitude fluctuations in the mass flux implied by the unstable mass entry model outlined in the previous section can be modeled as a steady flow, since the time variation scale of the mass flux (~ 0.5 s for Cen X-3) is far longer than the intrinsic photon bubble instability timescale (milliseconds). Therefore, our radiation hydrodynamic calculations, which assume steady flow on the photon bubble timescale, are directly applicable. Our identification of the high-frequency fluctuations in Cen X-3 (kilohertz QPO and broadband kilohertz continuum) with the photon bubbles (PBO and turbulence) is well supported by the fact that the four parameter radiation hydrodynamical simulations match the observations remarkably well in the applicable frequency range (> 100 Hz), with an adjustable polar cap size θ_c as the only free parameter of the fit. The mass of the neutron star, the magnetic field at its surface and the accretion rate are all constrained by other observations. Adjusting θ_c yields simulation calculations that qualitatively and approximately quantitatively explain 11 (of 15) free parameters of the best fit to the observed data. These include the form of the continuum power with a plateau, the high corner frequency and roll-off power law, and the presence of two broad lines (QPO) at the appropriate frequencies, amplitudes, and widths. The remaining four parameters of the fit to the observed data concern the low-frequency (< 100 Hz) behavior of the source and the PCA dead-time corrections. The range of applicability of the calculations does not include behavior of the source for frequencies below ~ 100 Hz. The mass entry model outlined above suggests that these low-frequency effects are related to modulation of the accretion rate due to the intrinsic instability of the mass entry mechanism, to which the X-ray emission from the surface passively responds. Thus, the match of the models to the observations lends strong support that our discovery of kilohertz fluctuations in the X-rays emitted by Cen X-3 can be identified with our prior suggestion that PBO would be observed in this X-ray source (Klein et al. 1996a).

The similarity between GRO J1744-28 and Cen X-3 is significant and strengthens the PBO identification for GRO J1744-28 (Klein et al. 1996b). Both GRO J1744-28 and Cen X-3 show two QPO peaks and a strong continuum in their power-density spectra (Zhang et al. 1996). The less complex pulse profile of GRO J1744-28 (nearly a perfect sinusoid) suggests a larger polar cap than for Cen X-3 in agreement with observations of lower frequency PBO/QPO. It is clear that the ~ 400 Hz separation in the kilohertz QPOs in Cen

X-3 has nothing to do with rotation since this separation frequency is vastly different than the 0.21 Hz spin frequency.

In contrast with the interpretation of GRO J1744-28, the identification of photon bubble phenomena in Cen X-3 is much firmer because of the naturally faster timescales extending to ~ 1800 Hz in the broad continuum. The observations reported here reaching to ~ 1800 Hz are the fastest known variations in the X-ray emission from an accreting compact object. We cannot exclude the simultaneous presence of additional mechanisms for temporal variability above 100 Hz but PB models provide the only mechanism that yields quantitative estimates for both amplitudes and frequencies.

Although the PB simulations include most of the accretion physics thought to be important near the surface of a neutron star undergoing optically thick accretion at the surface, there are some practical limitations. These models can currently only be integrated for a few tens of milliseconds, which limits a detailed comparison with averaged power-density spectra over days of exposure in an observed source. Future X-ray missions with significantly larger area detectors and parallelization of our algorithms would circumvent these difficulties.

Prior to the *RXTE* launch we predicted the observation of photon bubble phenomena including the specific existence of kilohertz fluctuations and some power in quasi-periodic oscillations identifiable as PBO in Cen X-3 (Klein et al. 1996a). We have now observed these fluctuations in

Cen X-3 and have refined the model calculations to match the actual frequency dependence of the power-density spectra including the presence of a significant continuum. A careful comparison of the predicted power density from the PB simulations with the observed power-density spectrum constrains the size of the polar caps of Cen X-3 to a radius of $\sim 2\text{--}3$ km. This has permitted the first model-dependent measurement of the size of the accreting polar cap in an X-ray pulsar.

The identification of PB phenomena in Cen X-3 opens the door to future X-ray observations with high-resolution timing that will allow us to probe the physics of the surface of super-Eddington accreting X-ray pulsars.

We acknowledge helpful conversations with Lars Bildsten, Lynn Cominsky, Saul Rappaport, and Will Zhang. We thank Ed Morgan for his extensive independent appraisal of the data analysis portion of the paper. We also thank both Ed Morgan and Wei Cui for providing the GX 17+2 data and the Cyg X-1 data respectively. These data were crucial for the development of a correct dead-time model of the PCA. This research has been supported by the award of a NASA ATP grant NAG 5-3809 and a NASA XTE Guest Observer grant NAG 5-3385. Part of this work was supported under the auspices of the US Department of Energy at the Lawrence Livermore National Laboratory under contract W-7405-Eng-48. The numerical models were calculated with the J90 supercomputers at LLNL.

APPENDIX A

PCA DEAD-TIME CORRECTIONS

In this appendix we describe the procedure for correcting the power-density spectrum for dead-time effects in the PCA. These corrections are required and are important in those cases in which the Leahy normalized power density falls below the level of 2 that is expected if no dead-time effects are present. We use a frequency-dependent model for an additive dead-time component of the power density of a form given by equation (6). This Leahy normalized dead-time model $P_{dt}(f)$ is suggested by equation (22) of Zhang et al. (1995) and equation (2) of Zhang et al. (1996) where f is the frequency. The functional form for the paralyzable and nonparalyzable dead-time models are nearly the same (compare Figs. 1 and 3 in Zhang et al. 1995). The practical distinction between the two models is insignificant below 10 kilohertz. The effect of discrete time binning is also unimportant below 10 kilohertz for the data shown in this appendix. The value of t_d is about $10\mu\text{s}$ and is a fixed property of the function of each of the five modules that comprise the PCA. The value of t_{vle} is a selectable parameter of the flight configuration of the PCA and is $\sim 61\mu\text{s}$ (level 1) or $\sim 142\mu\text{s}$ (level 2) for all data shown in this appendix. These selectable values of t_{vle} are averages of separate ground calibration measurements for the five PCUs of the PCA. The variations in these values of t_{vle} are of order 1%, which is more than sufficient for the purpose of evaluating dead-time corrections. The variables r_o and r_{in} are the actual counting rate and the incident counting rate (assuming no dead-time correction) respectively. The variable r_{vle} is the total rate of VLE (very large event) due to background particles and pileup of X-rays. These rates correspond to the values for one of the five PCA modules. Clearly the values of r_o and r_{in} are complex time-dependent functions as revealed by the actual observations of r_o . Equation (6) is suggested by the simple situation in which both r_o and r_{in} are constant. With further simplifying assumptions that $r_o \approx r_{in}$ and $r_o \ll t_d^{-1}$, we can express the values of A and B as approximate functions of the rates r_o and r_{vle} (see eqs. [7] and [8]). We will show that the overall dead-time correction $P_{dt}(f)$ can be successfully represented by fixed values of A and B for actual observations. Note that our proposed procedure for estimating the dead-time corrections is to vary the values of A and B as additional free parameters of any model that one might use to fit a power-density spectrum. The approximate relationship of A and B to any rates (r_o , r_{in} or r_{vle}) as given by equations [7] and [8] serves only as a verification for sensible values of A and B since these equations are based on a model that assumes that the rates are constant when in reality these rates are highly variable. Parameter C and third term of equation (6) is the additive component of background present in all PCA observations. Its functional form was determined by approximately (within about 1%) fitting the empirical power-density spectrum of a deep exposure to background with no significant sources present (E. H. Morgan 1999, private communication). This frequency-dependent function shows clear minima at 2000, 6000 and 10000 Hz and maxima at 0, 4000, and 8000 Hz. These features are likely produced by background events in channels 0–7 at a level of The total count rate from the background for GX 17+2, Cyg X-1, and Cen X-3 in channels 0–17 is $\sim 30\text{ s}^{-1}$. Since the background rate is not separately measured in the presence of a bright source there is no firm estimate of the background rate during an typical observation. The conservative procedure is to include an additive term in

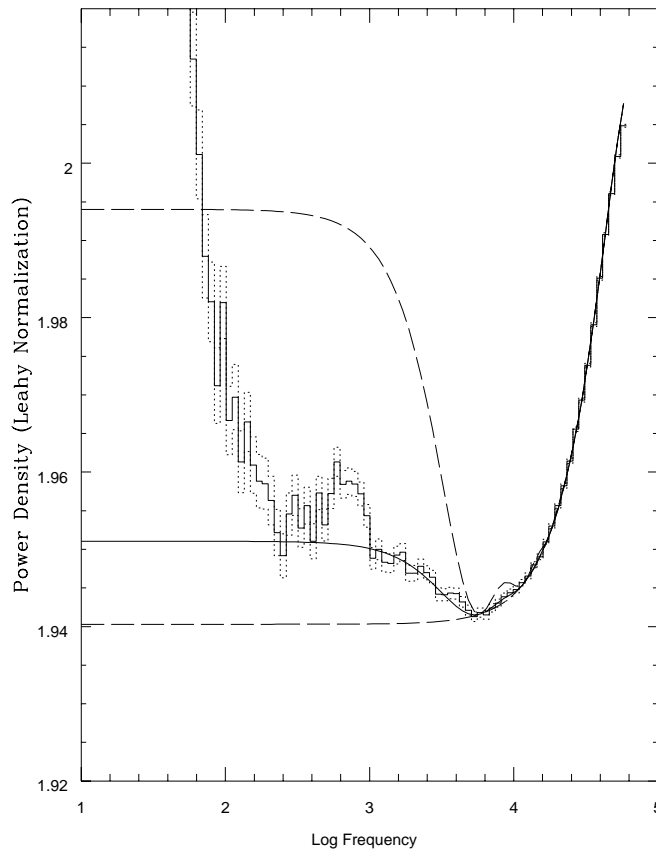


FIG. 5.—Power density of data from GX 17+2 over a frequency range that extends to ~50 kHz. The curve shows the Leahy normalized power density on a linear scale near the expected value of 2 as a function of the logarithm of the frequency. The value of the power density falls below 2 for frequencies greater than ~100 Hz clearly indicating that large dead-time corrections are necessary to determine the intrinsic component of the power density. The solid curve is an approximate fit of the dead-time corrected power density above ~2000 Hz as given by eq. (6), observed data is excellent above ~2000 Hz. The lower dashed curve shows the dead-time model if $B = 0$ with no VLE correction. The upper dashed curve shows the dead-time model if the VLE correction is arbitrarily increased by a factor of 6. This extreme form of the dead-time model shows a feature at ~9 kHz that is clearly in excess of the power-density level of the data. The correct dead-time model (*solid curve*) matches the slight “bump” in the power density near ~9 kHz.

the fit to any observe power spectra with an amplitude proportional to the parameter C. This background term is not really a dead-time correction but is included in the procedure since it is a model for the frequency-dependent form of a needed correction. In the worst case an error in the determination of the values of A, B, and C would correlate with some real component of the power-density spectrum of an observed source. This possibility always leads to an underestimate of the actual power-density spectrum of the source. Therefore this procedure, which freely varies the parameters A, B, and C, is a conservative approach for estimating any components of the power-density spectrum that are not real components of the observed target.

$$P_{dt}(f) = 2 - A \left[\frac{\sin(2\pi t_d f)}{2\pi t_d f} \right] + B \left[\frac{\sin(\pi t_{vle} f)}{\pi t_{vle} f} \right]^2 + 0.8744C(e^{-f/7900}) \left[\cos^2 \left(\frac{\pi f}{3950} \right) + 0.1436 \right], \quad (6)$$

$$A = 4(r_{in} t_d) e^{-r_{in} t_d} \approx 4t_d r_o, \quad (7)$$

$$B = 2(r_o t_{vle})(r_{vle} t_{vle}) \approx \frac{1}{2} A \left(\frac{t_{vle}}{t_d} \right) t_{vle} r_{vle}. \quad (8)$$

In Figure 5 we show the power-density spectrum of GX 17+2 over a frequency range that extends to ~50 kilohertz (E. H. Morgan 1999, private communication). The curve shows the Leahy normalized power density on a linear scale near the expected value of 2 as a function of the logarithm of the frequency. The value of the power density falls below 2 for frequencies greater than ~100 Hz, clearly indicating that large dead-time corrections are necessary to determine the intrinsic component of the power density. The solid curve is the dead-time component of the power-density spectrum, which approximately matches above ~2000 Hz, as defined by equation (6), with values of A and B equal to 0.0597 and 0.0101, respectively. The value of C is consistent with 0 indicating the low level of any background effects for source as bright as GX 17+2. The match of the dead-time model to the observed data is excellent above ~2000 Hz as indicated by the 1 σ error bars (*dotted stair-step curves*). In particular the broad dip in the power density near ~5000 Hz is fully explained as a dead-time correction due to VLE effects. The lower dashed curve shows the dead-time model if $B = 0$ with no VLE correction. The upper dashed curve

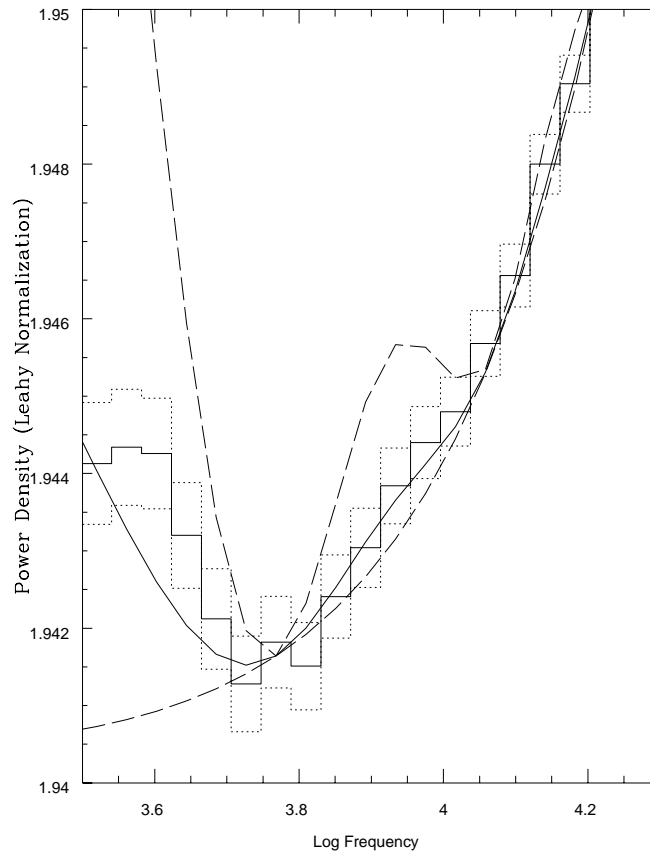


FIG. 6.—Figure is an expanded version of the data shown in Fig. 5. The purpose of this figure is to show clearly the match of the dead-time model to the slight bump in the power density at ~ 9 kHz. This feature corresponds to the second peak of the $[\sin(x)/x]^2$ function for the VLE correction to the dead-time model.

shows the dead-time model if the VLE correction is arbitrarily increased by a factor of 6. This extreme form of the dead-time model shows a feature at ~ 9 kilohertz, which is clearly in excess of the power-density level near that frequency. The correct dead-time model (solid curve) matches the slight “bump” in the power density near ~ 9 kilohertz. Figure 6 is an expanded version of the data shown in Figure 5. The purpose of this figure is to show clearly the match of the dead-time model to the slight bump in the power density near ~ 9 kilohertz. This feature corresponds to the second peak of the $[\sin(x)/x]^2$ function for the VLE correction to the dead-time model and therefore depends on the ground calibrated value of t_{vle} . The best values of A and B are approximately consistent with values of $r_o \sim 1500 \text{ s}^{-1}$ and $r_{\text{vle}} \sim 120 \text{ s}^{-1}$ for one of the five PCA modules. The implied total rates in the PCA are approximately consistent with the actual measured rates. The most conservative procedure for using this dead-time model is to allow the values of A and B to vary in order to match the high-frequency component of the power-density spectrum that is likely to be dominated by dead-time effects. One can then derive approximate values of r_o and r_{vle} by inverting equations (7) and (8) and then checking that these values are a rough match to the typical measured rates. With this interpretation of the dead-time correction Figure 5 shows the presence of the kilohertz QPO at ~ 600 Hz previously discovered by Wijnands et al. 1997 but no significant intrinsic power above ~ 1000 Hz. This dead-time corrected interpretation of the power-density spectrum of GX 17+2 shows for the first time that there is very little continuum power on either side of the kilohertz QPO feature. In summary, this power-density spectrum of GX 17+2 indicates that a simple dead-time model with two free parameters A and B successfully explains the frequency-dependent form of the dead-time correction to an accuracy of $\sim 1\%$ of the depression of the Leahy normalization 2 that is expected for pure Poisson noise with no dead-time correction.

Since our goal is to demonstrate that Cen X-3 shows excess power density in the range from 300–2000 Hz above the level of the dead-time correction, we seek an independent source of sufficient counting rate other than GX 17+2, which has no known intrinsic power in this frequency band. Figure 7 shows the power-density spectrum of Cyg X-1 over a frequency range that extends to ~ 6000 Hz. The data for the curve shown in Figure 7 were provided by W. Cui (1999, private communication) and show the Leahy normalized power density on a linear scale near the expected value of 2 as a function of the logarithm of the frequency. The value of the power density falls below 2 for frequencies greater than ~ 100 Hz, clearly indicating that dead-time corrections are necessary to determine the intrinsic component of the power density. The solid curve is an approximate fit of the dead-time corrected power density above ~ 300 Hz as given by equation (6). The approximate best values of A and B are 0.05 and 0.01, respectively, which corresponds to mean counting rate $r_o \sim 1250 \text{ s}^{-1}$ and $r_{\text{vle}} \sim 140 \text{ s}^{-1}$ for one of the five PCA modules. The implied total rates in the PCA are approximately consistent with the actual measured rates and are similar to the rates for GX 17+2. Again the background term (parameter C) is not needed because of the brightness of CYG X-1. The match of the dead-time model to the observed data is excellent above ~ 300 Hz. The lower

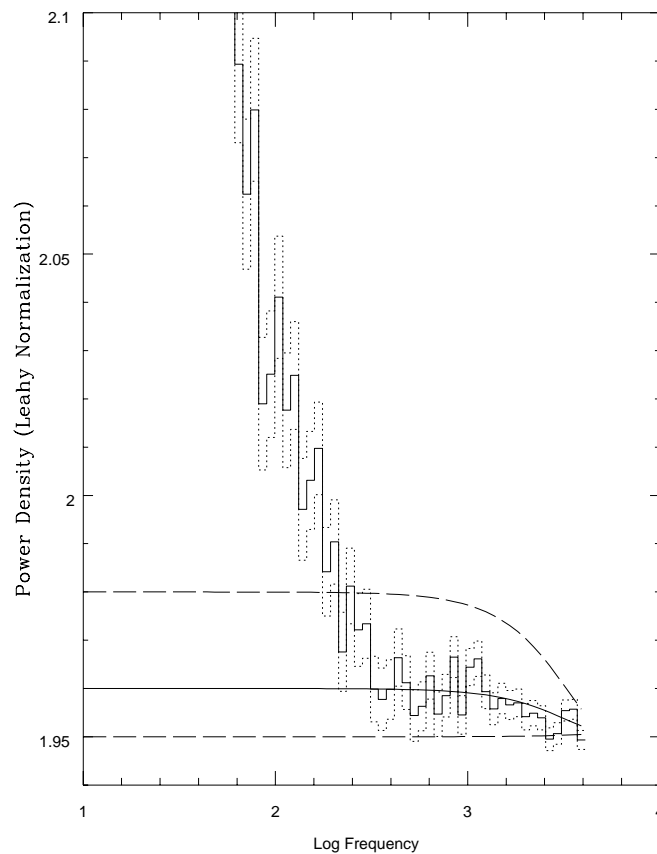


FIG. 7.—Power density of data from Cyg X-1 over a frequency range that extends to ~ 6000 Hz. The curve shows the Leahy normalized power density on a linear scale near the expected value of 2 as a function of the logarithm of the frequency. The value of the power density falls below 2 for frequencies greater than ~ 100 Hz clearly indicating that dead-time corrections are necessary to determine the intrinsic component of the power density. The solid curve is an approximate fit of the dead-time corrected power density above ~ 300 Hz as given by eq. (6), observed data is excellent above ~ 300 Hz. The lower dashed curve shows the dead-time model if $B = 0$ with no VLE correction. The upper dashed curve shows the dead-time model if the VLE correction is arbitrarily increased by a factor of 3.

dashed curve shows the dead-time model if $B = 0$ with no VLE correction. The upper dashed curve shows the dead-time model if the VLE correction is arbitrarily increased by a factor of 3, which is clearly inconsistent with the power-density spectrum. The dead-time corrected interpretation of this spectrum indicates the significant detection of intrinsic power from Cyg X-1 up to ~ 280 Hz. This interpretation extends and is consistent with prior published observations of Cyg X-1 (Cui et al. 1997; Nowak et al. 1999). For frequencies greater than ~ 300 Hz the spectrum is consistent with the dead-time model including the slight drop in power near ~ 2000 Hz. Since Cyg X-1 is a few times brighter than Cen X-3, these dead-time corrections will be greater than those for Cen X-3. The results for the Cyg X-1 data show that dead-time effects from 300–4000 Hz are smooth and correctable with no unexplained features. These data from Cyg X-1 were obtained in the similar PCA mode (SB_125us_0_17_1s) as the data from Cen X-3 reported in this paper (SB_62us_0_17_1s). In particular the energy range for the two data sets is identical. One could successfully use a scaled version of the spectrum of Cyg X-1 between 300–4000 Hz as the dead-time model for the Cen X-3 observations.

The stair step solid curve in Figure 8 shows the power density of data from Cen X-3 over a frequency range ~ 50 Hz to ~ 10 kilohertz. The stair step dotted curves above and below are the 1σ errors of the measured power density. These data are the same as shown in both Figures 1 and 2 and are plotted here to show clearly the level of the necessary dead-time correction.

The curve shows the Leahy normalized power density on a linear scale near the expected value of 2 as a function of the logarithm of the frequency. The value of the power density falls below 2 for frequencies greater than ~ 50 Hz, clearly indicating that dead-time corrections are necessary to determine the intrinsic component of the power density. The upper solid curve is the best fit model (15 parameters) to the total power density as a function of frequency. The range and best-fit values of each of the 15 parameters is shown in Table 2. Three of the parameters are the components A, B, and C of the dead-time model in the form given by equations (6), (7), and (8). The lower solid curve shows the dead-time model for the best fit values of A, B, and C (see Table 2). These data for Cen X-3 were obtained with a setting for t_{vle} of $\sim 61\mu\text{s}$ (level 1) in contrast a higher setting of $142\mu\text{s}$ (level 2) for the GX 17+2 and Cyg X-1 data. The lower setting decreases any VLE dead-time effect and was set to this lower value for the Cen X-3 observations precisely to decrease any VLE effect. The values of A and B are used to estimate typical values for r_o ($\sim 310\text{ s}^{-1}$) and r_{vle} ($\sim 40\text{ s}^{-1}$) which roughly agree with the observed average rates. The match of the dead-time model to the observed data is excellent above ~ 2 kHz. The lower dashed curve shows the dead-time model if $B = 0$ with no VLE correction. The upper dashed curve shows the dead-time model if the VLE correction is arbitrarily increased by a factor of 6. Such a model roughly matches the level of the power density in the frequency range from

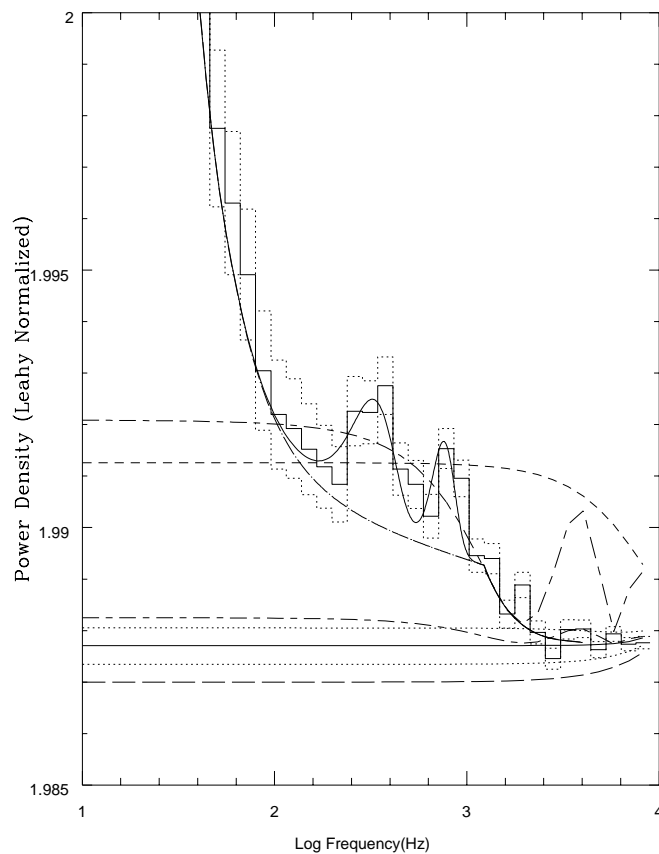


FIG. 8.—Power density of data from Cen X-3 over a frequency range ~ 50 Hz to ~ 10 kHz is the stair step solid curve. The stair step dotted curves above and below are the 1σ errors of the measured power density. These data are the same as shown in both Figs. 1 and 2 and are plotted to show clearly the level of the necessary dead-time correction. The curve shows the Leahy normalized power density on a linear scale near the expected value of 2 as a function of the logarithm of the frequency. The upper solid curve is the best fit model (15 parameters) to the total power density as a function of frequency. The lower solid curve is the best fit of the dead-time correction to the power density. The match of the dead-time model to the observed data is excellent above ~ 2 kHz. The lower dashed curve shows the dead-time model if $B = 0$ with no VLE correction. The upper dashed curve shows the dead-time model if the VLE correction is arbitrarily increased by a factor of 6. The dotted continuous curves just above and below the lower solid curve show the effect on the dead-time model if the VLE correction factor (parameter B) is varied from a low to a high value that corresponds to a 50% confidence range. The continuum component (see *dashed-dotted curve*) is well above the level of the dead-time component (*lower solid curve*).

100–1000 Hz but is completely inconsistent with the power density from 1–10 kHz. Clearly the excess power density in the frequency range 100–2000 Hz cannot be explained as a VLE dead-time effect. The dotted continuous curves just above and below the lower solid curve show the affect on the dead-time model if the VLE correction factor (parameter B) is varied from a low to a high value corresponding to the 50% confidence range. A correct VLE dead-time correction does effect the determination of the intrinsic level of the continuum power in the 100–1000 Hz range. However the continuum component (see *dashed-dotted curve*) is well above the level of the dead-time component (*lower solid curve*). The lower short-dash–long-dash curve is the upper limit to the background as determine by the free parameter C. It shows a drop at 2000 Hz followed by a small peak at 4000 Hz that reaches but does not exceed the measured power density at 4000 Hz. This upper limit for C greatly exceeds any expected level of the background that is likely at least full order of magnitude lower. Even so, a value of C that is increased by a factor 8 (see the upper short-dash–long-dash curve) does roughly match the overall shape of the power-density spectrum from 100–2000 Hz. This artificially amplified value of C would create a strong peak at 4000 Hz, which is well above the measured level of the power density near 4000 Hz. Estimates for the contribution of the background are also shown in Figure 1. An additive background contribution is not a significant component of the power-density spectrum of Cen X-3.

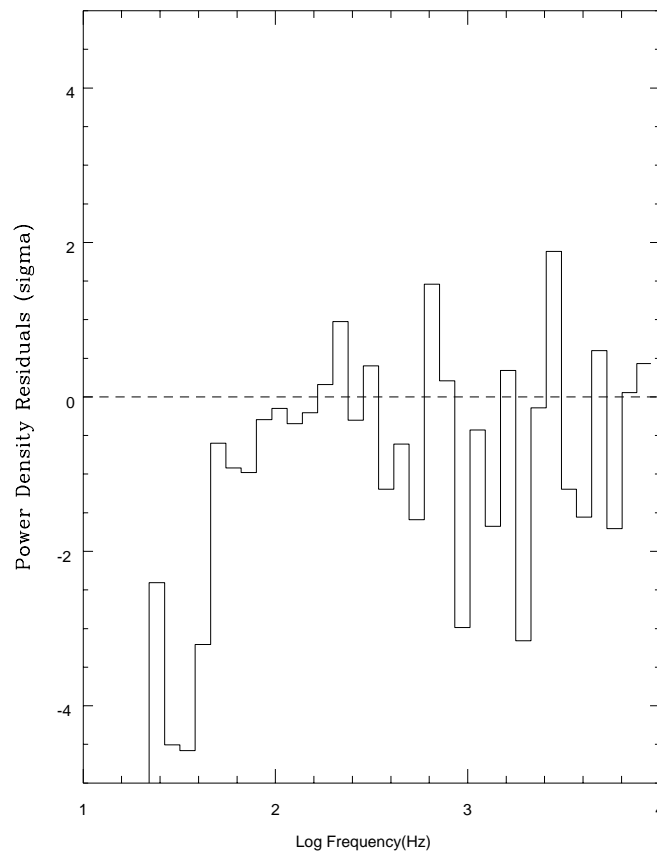


FIG. 9.—Power-density residuals of data from Cen X-3 over a frequency range ~ 50 Hz to ~ 10 kHz is the stair step solid curve. The model minus data residuals are plotted in units of the local measured 1σ error for each data point. These model and data are the same as shown in Fig. 8. The model approximately uniformly fits the data above ~ 100 Hz and therefore all parameters related to the kHz QPO and continuum are formally well defined. The power-law model below ~ 100 Hz is clearly not sufficiently complex to completely model the behavior of Cen X-3 at low frequency. This difficulty with the model is amplified by the excellent signal to noise below ~ 100 Hz.

REFERENCES

- Arons, J. 1992, *ApJ*, 388, 561
 ——— J. 1993, *ApJ*, 408, 160
 Arons, J., & Lea, S. 1980, *ApJ*, 235, 1016
 Arons, J., Klein, R. I., & Lea, S. M. 1987, *ApJ*, 312, 666
 Arons, J., & Lea, S. M. 1976, *ApJ*, 207, 914
 Baym, G., & Pethick, C. 1979, *ARA&A*, 17, 415
 Belloni, T., & Hasinger, G. 1990, *A&A*, 230, 119
 Bildsten, L., et al. 1997, *ApJS*, 113, 367
 Bradt, H. V., Rothschild, R. E., & Swank, J. H. 1993, *A&AS*, 97, 355
 Burnard, D. J., Lea, S. M., & Arons, J. 1983, *ApJ*, 266, 175
 Cui, W., Zhang, S. N., Focke, W., & Swank, J. H., 1997, *ApJ*, 484, 383
 Davidson, K., & Ostriker, J. P. 1973, *ApJ*, 179, 585
 Elsner, R. F., & Lamb, F. K. 1977, *ApJ*, 215, 897
 ———. 1984, *ApJ*, 278, 326
 Giacconi, R., Gursky, H., Kellogg, E., Schreier, E., & Tananbaum, H. 1971, *ApJ*, 167, L67
 Ghosh, P., & Lamb, F. K. 1979, *ApJ*, 232, 259
 Hawley, J. F., Gammie C. F., & Balbus, S. A. 1995, *ApJ*, 440, 742
 Hutching, J. B., Cowley, A. P., Crampton, D., van Paradijs, J., & White, N. E. 1979, *ApJ*, 229, 1079
 Klein, R. I., & Arons, J. 1989, in Proc. 23rd ESLAB Symp. on Two Topics in X-Ray Astronomy, ed. N. E. White & T. D. Guyenne (ESA SP-96; Paris: ESA), 1, 89
 ———. 1991, in *Stellar Atmospheres: Beyond Classical Models*, L. Crivillari, ed. (Boston: Kluwer), 205
 Klein, R. I., Arons, J., Jernigan, G., & Hsu, J. 1996a, *ApJ*, 457, L85
 Klein, R. I., Jernigan, G., Arons, J., Morgan, E. H., & Zhang, W. 1996b, *ApJ*, 469, L119
 Lamb, F. K., Pethick, C. J., & Pines, D. 1973, *ApJ*, 184, 271
 Lampton, M., Margon, B., & Bowyer, S. 1976, *ApJ*, 208, 177
 Lazarian, A., & Vishniac, E. T. 1999, *ApJ*, 517, 700
 Leahy, J. A., Darbo, W., Elsner, R. F., Weisskopf, M. C., Sutherland, P. G., Kahn, S., & Grindlay, J. E., 1983, *ApJ*, 266, 160
 Nowak, M. A., Wilms, J., Vaughan, B. A., Dove, J. B., & Begelman, M. C. 1999, *ApJ*, 515, 726
 Pringle, J. E., & Rees, M. J. 1972, *A&A*, 21, 1
 Rappaport, S., & Joss, P. 1983, in *Accretion Driven Stellar X-ray Sources*, ed. W. H. G. Lewin & E. P. J. van den Heuvel (Cambridge: Cambridge Univ. Press)
 Santangelo, A., Sordo, S. D., Segreto, A., Fiume, D. D., Orlandini, M., & Piraino, S., 1998, *A&A*, 340, L55
 Schreier, E. J., Giacconi, R., Gursky, H., Kellogg, E., & Tananbaum, H. 1972, *ApJ*, 178, L71
 Swank, J. H. 1997, *Nucl. Phys. B Proc. Suppl.* 69, 12
 Taam, R. E., & Spruit, H. C. 1990, *A&A*, 229, 475
 van der Klis, M., Jansen, F., van Paradijs, J., Lewin, W. H. G., Trumper, J. E., & Sztajno, M. 1995a, *IAU Circ*, 4043, 1
 van der Klis, M., Jansen, F., van Paradijs, J., Lewin, W. H. G., van den Heuvel, E. P. S., Trumper, J. E., & Sztajno, M. 1995, *Nature*, 316, 225
 Wijnands, R., et al. 1997, *ApJ*, 490, L157
 Zhang, W., Jahoda, K., Swank, J. H., Morgan, E. H., & Giles, A. B. 1995, *ApJ*, 449, 930
 Zhang, W., Morgan, E. H., Jahoda, K., Swank, J. H., Strohmayer, T. E., Jernigan, G. & Klein, R. I. 1996, *ApJ*, 469, L29